### Title
Impact of Dispersion Solvent on Ionomer Thin Films and Membranes

### Permalink
https://escholarship.org/uc/item/6n78v97h

### Journal
ACS Applied Polymer Materials, 2(12)

### ISSN
2637-6105

### Authors
Berlinger, Sarah A
Dudenas, Peter J
Bird, Ashley
et al.

### Publication Date
2020-12-11

### DOI
10.1021/acsapm.0c01076

Peer reviewed

# Impact of Dispersion Solvent on Ionomer Thin Films and Membranes

*Sarah A. Berlinger[1,2,*], Peter J. Dudenas[1,2,†], Ashley Bird[1,2], Xunkai Chen[1,2], Guillaume Freychet[3], Bryan D. McCloskey[2], Ahmet Kusoglu[1], Adam Z. Weber[1]*

[1]Energy Conversion Group, Lawrence Berkeley National Laboratory, Berkeley, CA 94720,

[2]Department of Chemical and Biomolecular Engineering, University of California, Berkeley, Berkeley, CA 94720

[3]National Synchrotron Light Source II, Brookhaven National Laboratory, Upton, NY 11973

## ABSTRACT

Perfluorosulfonic-acid (PFSA) ionomers are an important class of materials that many electrochemical devices rely on as their ion-conducting electrolyte. Often, PFSA films are prepared through solution-processing techniques. Previous research has demonstrated that the solvent environment affects PFSA dispersion conformation, but it is not clear to what extent (if at all) these conformational effects persist for thin films and membranes upon casting, nor how dispersion solvent impacts film formation during the drying process. Here, we explore these questions by systematically examining the effect of water and n-propanol mixtures on PFSA thin-film formation and structure, membrane structure, and resulting properties. Using a combination of *in situ*, time-resolved Grazing Incidence X-ray Scattering and tender Wide Angle X-ray Scattering, it is shown that films prepared from high-water-concentration dispersions exhibit stronger interactions and arrangement upon drying and possess larger network domain sizes than those prepared from low-water-concentration dispersions. These stronger interactions likely manifest in greater network connectivity as evidenced by enhanced conductivity for membranes and decreased water uptake for thin films. Significantly, these solvent-induced differences persist even after thermal annealing. It is clear dispersion solvent choice is a critical parameter controlling PFSA nano- and mesoscale structure and presents an important dial with which to direct PFSA macroscale properties.

KEYWORDS: Perfluorosulfonic acid; ionomer; solvent; thin film; membrane; dispersion; fuel cells; X-ray scattering

## INTRODUCTION

Perfluorosulfonic acid (PFSA) ionomers are a critical component of many energy-conversion devices, including proton-exchange-membrane fuel cells and electrolyzers. In these devices, PFSA is present both as a membrane separating the anode from cathode, as well as incorporated into the catalyst layers (CLs). In the CLs, PFSA exists as thin films (on the order of tens of nanometers) covering catalyst-particle agglomerates, serving as a binder for CL structure while providing critical ionic pathways.[1] PFSA consists of a hydrophobic polytetrafluoroethylene backbone with pendant sidechains that terminate in sulfonic-acid groups (structure shown in Figure S1 in the SI). The hydrophobic and hydrophilic regions of the polymer nanophase separate into backbone-rich domains that lend mechanical support, interspersed with water domains that allow for ion and water transport. The mechanical and transport properties of PFSA, particularly in bulk-membrane form, have been extensively characterized.[2]

Despite the wealth of literature investigating PFSA membrane properties, the impact of solution processing on PFSA has received considerably less attention. Understanding how various solution parameters affect cast (dried) PFSA films has significant implications for device performance, particularly as it relates to the CLs. The CLs are manufactured through solution-based colloidal slurry (ink) techniques, in which the ionomer and catalyst particles are dispersed in a solvent, and then cast and dried to form the resulting electrode.[3] The properties of the ink directly impact the CL; the strong effect of changing ink solvent on device performance has been demonstrated for proton-exchange-membrane (PEM) fuel-cell CLs.[4-16] These solvent effects are attributed to changing ionomer/catalyst particle interactions within the ink; ionomer aggregation behavior and coverage on the catalyst surface changes as a function of ink solvent.[4-5] Clearly, solvent impacts PFSA behavior. Additional ink-level studies have explored this phenomenon: solvent type alters ink properties, affecting important metrics such as aggregate size, zeta potential, and rheological behavior due to changing ionomer/solvent/particle interactions.[3, 17-20]

These studies are important steps toward understanding how solvent affects CL microstructure and performance. However, the multi-component interactions present within an ink are incredibly complex, and ink-level studies provide limited information as it pertains to the ionomer. For example, some unanswered questions are: How is the ionomer changing as a function of solvent, and why? How does solvent control film formation? How do these differences manifest upon casting? Much of the fundamental challenges in the CLs are associated with the ionomer/catalyst-particle interface. Elucidating how the ionomer is affected by solvent during the casting process is crucial to understand and control this interface. Additionally, beyond CLs, polymer-solution processing across all fields is becoming increasingly utilized due to the ease of manufacturing and scalability (especially with aqueous solvents).

Several studies have recognized the need to understand ionomer/solvent interactions and have focused on PFSA dispersion[1] properties. In most solvent systems, PFSA can be thought of as a colloidal dispersion due to solvent/backbone incompatability.[21] A few PFSA chains will come together to form primary aggregates, the structure of which is dictated by the solvent environment. These primary aggregates (~angstroms to nanometers) determine the primary Nafion particle shape. These can then aggregate further into secondary aggregates (~100's of

---

[1] For the rest of this paper we mean dispersion to describe a solvent/PFSA mixture, as opposed to an ink that incorporates catalyst particles

nanometers). In polar solvents, PFSA aggregates into rod-like structures, with radii on the order of tens of angstroms.[22-24] Secondary aggregation modes then vary depending on solvent, even when considering only polar solvents. Small-angle neutron-scattering work revealed that water/alcohol mixtures yield very different ionomer secondary aggregate conformations (swollen particles) than alcohol alone (bundles), and solvents like N-Methyl-2-pyrrolidone produce a more classical random coil characterized by a radius of gyration.[21] Water/alcohol mixtures are particularly relevant for CL applications, and as such have been the focus of a few studies.[9, 18, 25-27] pH measurements suggest that as the proportion of water relative to alcohol increases, the ionomer sidechains extend into solution and the backbone clusters in the middle of the secondary aggregate much like a micellar structure,[18] as confirmed by molecular-dynamics simulations.[27]

Other studies have focused on how solvent affects solution-cast PFSA membranes[28-32], and have shown that the degree of aggregation in the dispersion (due to the ionomer conformation that is affected by dielectric constant and solubility parameters[29]) impacts the membrane's structure, and the degree of phase separation when cast.[28] However, these studies rarely use industrially-relevant solvents (water-alcohol mixtures are often preferred due to ease of use, cost, and safety), and have little understanding about the mechanism of film formation or impact of solvent on thin films. Important recent work probes PFSA thin-film formation;[33] however, the effects of solvent remain unknown.

In this paper, we systematically study the impact of dispersion solvent (varying water to alcohol ratios) on the *in situ* evolution of film morphology from dispersion to thin film via Grazing Incidence Small Angle X-ray Scattering (GISAXS). We extend this information across length scales, looking at the final structures of both thin films and membranes, and how these structures impact important metrics such as swelling/water uptake and ionic conductivity. Finally, we investigate whether these differences are retained after high-temperature processing. In this way, we correlate important structure-property-processing relationships that govern PFSA thin films and membranes.

## EXPERIMENTAL

**Dispersions.** All dispersions used in this study contained 4 wt.% Nafion (the prototypical PFSA) dispersed in varying ratios of water to n-propanol (nPA) ranging from 90 wt.% water to 30 wt.% water (balance nPA) except where noted. The dispersions were prepared by diluting stock 20 wt. % dispersion (D2021, equivalent weight 1100 g polymer/mol sulfonic-acid groups, Ion Power, Inc.) to the appropriate concentration using water and nPA, considering the native solvent in the stock dispersion. Upon dilution, dispersions were mechanically mixed and then sonicated for 30 minutes in a bath sonicator (Branson) equipped with a custom temperature control system to maintain room temperature. Dispersion rheology was measured using a 40 mm parallel plate geometry with an 800 μm gap on a Discovery Hybrid Rheometer 2 (TA Instruments).

**Thin Films.** *In situ* casting experiments of thin films were conducted at beamline 7.3.3 of the Advanced Light Source at Lawrence Berkeley National Laboratory. Dispersions used here were prepared at 2 wt.% Nafion in an identical manner as described above. Dispersions were cast *in situ* using a custom-built mini slot-die printer.[34] After priming the line with solution, the films were cast from the slot-die head onto a silicon wafer with a head-substrate gap height of 200 μm and an injection rate of 5 μL/s, such that a similar volume of dispersion was dispensed for each sample. Silicon was chosen as a model substrate.[2] The print head was stationary while the substrate was translated underneath at a rate of 5 mm/s for the 90%, 70%, and 50% water dispersions and 2.5 mm/s for the 30% water dispersion. The X-ray energy was 10 keV ($\lambda$=1.24 $A^{-1}$) with a monochromator energy resolution $E/\Delta E$ of 100, and the patterns were acquired with a Dectris Pilatus 2M CCD area detector (172 μm x 172 μm pixel size) at a sample-to-detector distance of 2.515 m. GISAXS images were collected at grazing incidence angles ($\alpha_i$) of 0.16° with 1 sec exposure under ambient atmosphere. Through-plane linecuts were averaged at $q_p$=0.3 ± 0.05 $nm^{-1}$, and horizontal linecuts were averaged at $q_z$=0.25 ± 0.05 $nm^{-1}$. Linecuts were fit to a core-shell model using the NCNR SANS Toolbox.[35] The Teubner-Strey model[36-37] was fit using scripts written in python, and error bars on the extracted parameters represent one standard deviation. Exposure times and total dose were selected to mitigate x-ray induced damage to the sample, while capturing the relevant drying dynamics.

Swelling (water-uptake) measurements were conducted on thin films. The thin films were prepared by spin casting the dispersions on silicon wafers (as in the casting experiments). The wafers were first cleaned with UV/ozone for twenty minutes to make them more hydrophilic prior to spin casting. Initial film thickness for all samples was measured with spectroscopic ellipsometry (J. A. Woollam alpha-SE) to be roughly 140-150 nm. Both annealed and unannealed samples were prepared. Annealed samples were placed in a 150°C vacuum oven for one hour before being removed. Unannealed samples were similarly dried in a vacuum oven for one hour, but at 30°C before being removed, and measured immediately for the swelling measurements. These measurements were conducted by monitoring the transient thickness as a function of relative humidity (RH) using a spectroscopic ellipsometer at an incident angle of 70°. The wave amplitude ($\Psi$) and phase shift ($\Delta$) were measured over a spectral range of 400-900 nm and fit to a three-layer optical model (Si, native $SiO_2$, and Cauchy layer). The samples were exposed to nitrogen saturated at various RHs flowing at 500 $cm^3$ $min^{-1}$: first with a conditioning cycle of 0 to 100 to 0% RH for 1 hour each at each step, then an absorption cycle of 10 to 100% RH, in increments of 10%, for a half hour each. Two of these absorption runs were measured for each sample to test repeatability. Data was averaged over multiple films. Swelling (*ΔL*) was determined by calculating the change in thickness at each RH step relative to the thickness at the end of the second 0% RH step in the conditioning cycle ($L_0$). To convert swelling data to water content ($\lambda$, moles of water per mole sulfonate groups), one-dimensional swelling was assumed (i.e. that the films swell only in the thickness direction because they are confined to the substrate)[38]; assuming no significant excess free volume or macroscale voids exist and additive partial molar volumes is valid[38-42] yields

$$\lambda = \frac{mol\,H_2O}{mol\,SO_3^{-¿} = \frac{\Delta L}{L_0}\,\frac{\rho_W / MW_W}{\rho_N / EW}¿} \qquad (SEQ\ 1)$$

where subscripts *W* and *N* denote water and Nafion, respectively, $\rho$ is dry density, MW is molecular weight and EW is the equivalent weight of Nafion (here 1100 g polymer/mol sulfonic-acid groups). A dry density of 2.1 g/$cm^3$ was used for Nafion.[43-44]

**Membranes.** Membranes were fabricated from the same dispersions as described above. The dispersions were poured into custom-made glass wells such that the same mass of ionomer was added to each. They were then heated at 35 °C for 1 hour and annealed at 150 °C for an additional hour, before slowly cooling back to room temperature overnight. They were then carefully removed from the glass, and the dry thickness of all membranes was measured at 16 +/-

2 μm with a thickness gauge (Heidenhain). Separate membranes were measured with tender x-ray scattering to quantify structure, and to measure water uptake and conductivity. For the property measurements, the membranes were cut in half: one portion was stored in air for water-uptake measurements, and the other was immersed in MilliQ (18 MΩ de-ionized) water to equilibrate for liquid-water conductivity measurements.

Sulfur K-edge scattering measurements were performed at the Soft Matter Interfaces (SMI, Beamline 12-ID) at the National Synchrotron Light Source II.[45] Samples were measured in transmission mounted perpendicular to the beam. X-ray scattering patterns were recorded on a Pilatus 300K-W detector, consisting of 0.172 mm square pixels in a 1475 × 195 array, mounted at a fixed distance of 0.275 m from the sample position. To cover the range of scattering angles desired, the vertically oriented elongated detector was moved horizontally on a fixed arc, from 0 to 26 degrees with 6.5 deg steps. Scattering patterns, recorded in-vacuum, were measured at 2542 eV. Images were later visualized in Xi-CAM software[46] and stitched using custom python code. The spot size at the sample was 20 μm by 200 μm.

Membrane water uptake as a function of RH was measured with a dynamic vapor-sorption (DVS) analyzer (Surface Measurement Systems, UK) at 25 °C.[47-48] The samples were first dried at 25°C and 0% RH for 2 hours to determine the dry mass of the membrane $M_0$. The water uptake ($\Delta M_W$) was then continuously measured as RH increased from 0 to 98% with a 10% RH interval using a pre-humidified nitrogen feed. Membranes were equilibrated at each RH step until the mass change with respect to the initial mass ($\Delta M_W/M_0$) had less than 0.005% change per minute. The water content was calculated from the water uptake according to

$$\lambda = \frac{\Delta M_W / MW_W}{M_0 / EW}$$

(

*SEQ*

2)

The residual water ($\lambda_{res}$) present in the membrane at 25°C and 0% RH was calculated in the same way, by comparing the mass change after 2 hours at 120°C relative to the initial mass at 25 °C.

Membranes used for the conductivity measurements were equilibrated in DI-water for 24 hours before their wet thickness and width were measured. The resistance of the membranes was then measured using a four-point probe (BekkTech) and potentiostat (BioLogic) to sweep the voltage from -0.1 to 0.1 V and record the current as described previously.[49] Conductivity was calculated from the resistance measurement using the dimensions of the cross-sectional area of the membrane and the spacing between the electrodes. Four different membranes for each solvent ratio were measured.

## RESULTS & DISCUSSION

### **Structure**

*Thin-Film Evolution.* To understand the effect of dispersion solvent on film formation, structure, and properties across length scales, four different ratios of water:n-propanol (nPA) are used throughout this study. All samples are made from Nafion (a prototypical PFSA) dispersions that have a solvent composition of 90:10, 70:30, 50:50, or 30:70 all given as wt.% water:wt.% nPA and hereafter referred to as 90, 70, 50, and 30% water samples, respectively. The thin-film morphological formation was accomplished by *in situ* GISAXS experiments, in which the Nafion dispersion is cast onto a silicon substrate via a slot-die printer and the structure monitored with time as described previously.[33]

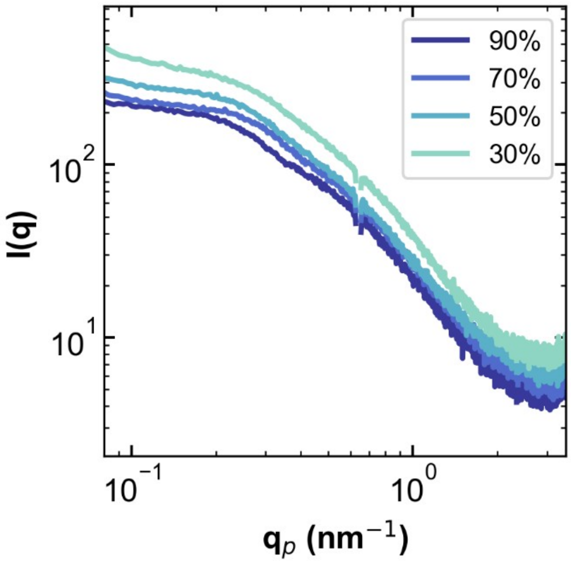

**Figure 1.** In-plane linecuts describing intensity (I) as a function of the scattering vector ($q_p$) obtained from *in situ* GISAXS experiments of the dispersions immediately upon casting. Labels describe the weight percentage of water that makes up the dispersion solvent composition (the balance is n-propanol).

Figure 1 shows the initial horizontal intensity linecuts obtained immediately after printing the dispersions, plotted versus the in-plane scattering vector ($q_p$). Similar results were obtained for the through-plane scattering and are shown in Figure S2 in the SI. Previous work showed that the primary particle adopts a rod-like conformation in similar solvents.[22, 33] Using the same modeling/analysis approach, these initial linecuts are fit to a cylindrical core-shell form factor in the high-q region ($q_p > 0.7$ nm$^{-1}$), where the structure factor is expected to approach 1. The form-factor fit is shown in Figure S3 (in the SI) with excellent agreement (fit parameters are shown in

Table S1 in the SI). The core-shell form factor is not expected to change much with drying (i.e. the primary particle should remain intact due to the highly hydrophobic PTFE core) and the form factor is therefore held constant during subsequent analysis. Changes in the core-shell length may occur, but the form factor is relatively insensitive to length in this q-range.

There are small differences in the shell thickness with water:nPA ratio, but this change is mostly within error of the fit (Figure S4 in the SI). To further reduce the error and determine a clear trend in shell thickness with water:nPA ratio, wide-angle x-ray scattering would need to be done to access q = 4-10 $nm^{-1}$. Greater differences in the scattering for each of the samples is observed at lower q. The upturn in intensity at $q_p < 0.1$ $nm^{-1}$ varies between water:nPA ratios, and indicates differences in the formation of larger length scale secondary aggregates of Nafion in all dispersions, as suggested by many previous studies.[18, 21] Between $q_p$ = 0.1 and 0.7 $nm^{-1}$, differences in the scattering suggest differences in intermediate length scale aggregation and the structure factor.

These initial linecuts can be divided by the form factor to generate an effective structure factor ($S_{eff}$, Equations S1-3 in the SI). We call it an effective structure factor because it is not known *a priori*, but instead is derived from scattering. Initial structure factors for all solvent ratios are shown in Figure S5 of the SI. The primary structure-factor peak around 0.3-0.4 $nm^{-1}$ is evident for all dispersions. This same calculation is performed for the rest of the time-resolved data: $S_{eff}$ is analyzed at all time points during the drying process. The intensity of the in-plane and through-plane structure factor peaks is shown in Figure 2 as a function of time during the initial portion of the drying process.

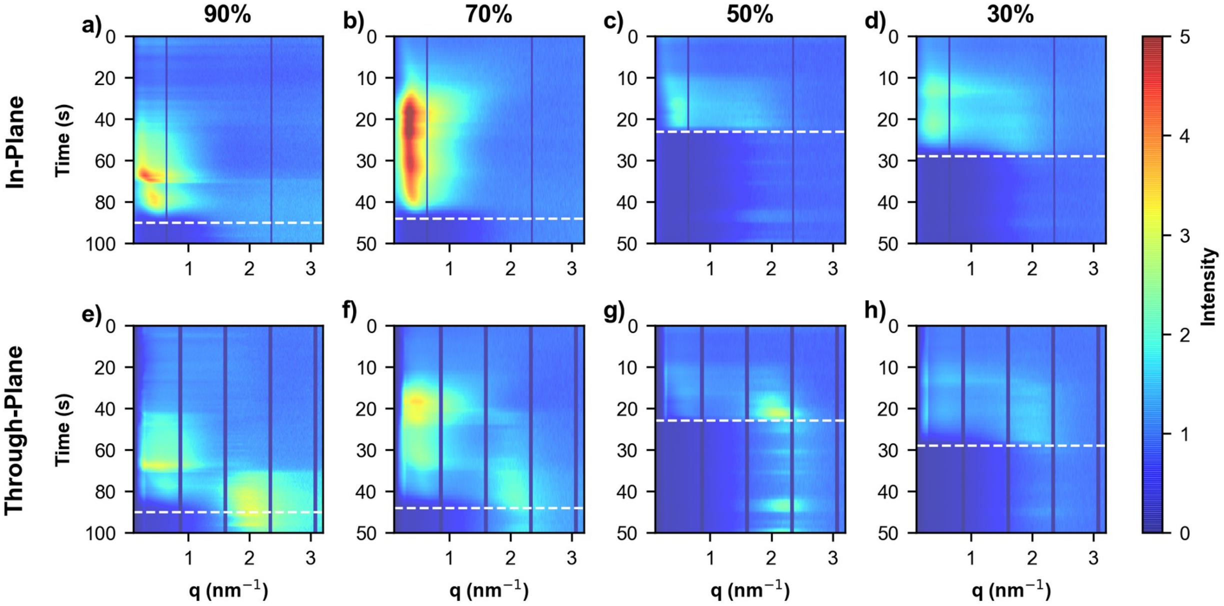

**Figure 2**. Effective structure factor ($S_{eff}$) time evolution of the sol-gel transformation both (a)-(d) in-plane and (e)-(h) through-plane for the dispersions after casting for dispersion solvents containing (a, e) 90%, (b, f) 70%, (c, g) 50%, and (d, h) 30% water (balance nPA). Note the 90% sample has a different y-scale. Dashed white line indicates gel formation.

As shown in previous work, the first portion of the drying process is a solution-to-gel transformation.[33] Gelation is evidenced by the collapse of the primary structure factor peak around 0.3-0.4 nm$^{-1}$ (noted by a lack of contrast) and is indicated by a dashed white line on each heat map in Figure 2. Immediately obvious is the fact that the high-water-concentration dispersions (HWD, 90% and 70%) take longer to form and dry than the low-water-concentration dispersions (LWD, 50% and 30%). The solution-to-gel transformation was determined for each water concentration as the time at which the following linecut does not change in this q-range. The primary structure-factor peak describes how the dispersion particles (both primary and secondary aggregates) are arranged in solution relative to one another.[33] As the dispersion gels, the particles begin to coalesce and the primary peak moves to higher q. As gelation completes, the main structure factor peak disappears.[33] The much longer drying time for the HWD as compared with the LWD is expected when considering the relative volatility of water and nPA.

Another qualitative observation can be made about the intensity of the structure factor peaks: the primary structure-factor evolution is much stronger for the HWD than the LWD. This increased intensity indicates a greater regularity to the arrangement of aggregates in solution, and stronger interaction between the aggregates. These Nafion/Nafion interactions were probed *ex situ* using rheology as shown in Figure 3, where the relative viscosity (measured viscosity of the dispersion divided by the viscosity of the solvent) at the same shear rate that the dispersions were cast with the slot-die coater (see SI Figure S7 for the full measured viscosity range and shear-rate calculations). Figure 3 displays an increase in relative viscosity with dispersion water concentration. Generally, increased viscosity and non-Newtonian behavior indicates stronger polymer/polymer interactions;[50] the HWD exhibit greater degrees of shear-thinning than the LWD (as seen in Figure S7). Here, these stronger interactions are likely electrostatic in nature due to higher Nafion acidity in water-rich dispersions[18] and longer electrostatic correlation lengths. Another reason for increased viscosity could be smaller particle sizes (since the dispersions all possess the same polymer concentration, this would cause a relative increase in volume fraction).[50] Smaller particles (less secondary aggregation) could also be a result of the greater electrostatic repulsion experienced by water-rich dispersions as compared with n-propanol-rich ones. While particle size versus particle/particle interaction contributions to the viscosity cannot be explicitly deconvoluted by this experiment, these results help explain the stronger structure factor peak in the HWD: increased interaction between particles enhances ordering.

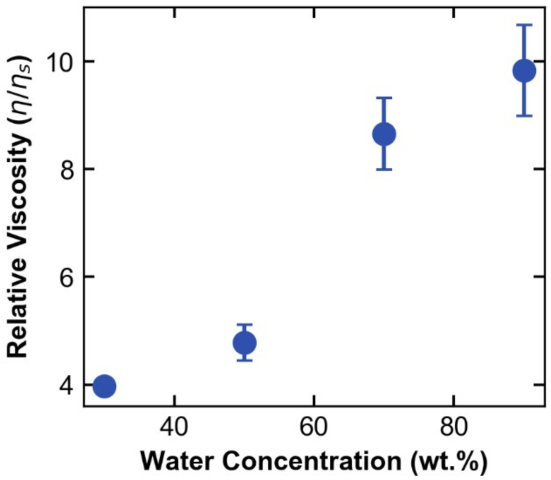

**Figure 3**. Measured viscosity of 4 wt. % Nafion dispersions (η) divided by the pure solvent viscosity ($\eta_s$) as a function of the water concentration in the dispersion (balance n-propanol) at ~12 Hz (the shear rate used to print the films for the *in situ* casting experiments).

We have so far discussed the primary structure-factor peak, but there is also a secondary structure-factor peak around 2 $nm^{-1}$ corresponding to correlation lengths of 3 to 4 nm. This secondary structure-factor peak most likely describes the secondary aggregates in the system.[33] A further discussion of the assignment of structure factor peaks is presented in the SI. Notably, this secondary structure-factor peak is absent at short drying times for the HWD through-plane, and does not appear in-plane, as opposed to the LWD, for which this secondary aggregate peak is present in both directions for a much longer portion of the drying time. When considering charged particle aggregation theories, primary aggregates are stable (and do not become secondary aggregates) when there is sufficient electrostatic/coulombic repulsion to keep them apart. It is expected that the HWD would experience greater electrostatic repulsion, and therefore have a larger energy barrier to overcome in order to form secondary aggregates. The HWD display more acidic[18] (more charged) conformations, and the increased dielectric constant of the solvent media would similarly increase the magnitude of electrostatic repulsion experienced by the aggregates. Additionally, the smaller particle size as suggested by the viscosity measurements further indicate that the HWD have trouble forming secondary aggregates initially. However, as the solvent evaporates, Nafion concentration increases. This increases the relative ionic strength of the system, and therefore decreases the electrostatic repulsion and accordingly the height of the energy barrier, thus explaining why the secondary structure-factor peak does not appear until later times for the HWD.

Following the solution-to-gel transformation, Nafion particles continue to coalesce as solvent evaporates.[33] In the gel state, the secondary structure-factor peak collapses into the well-known ionomer peak.[33] Here, as the gel continues to dry, there are some oscillations in intensity, which may be due to heterogeneous drying (i.e. coffee-ring effect), or re-entrant solvent from the static headspace above the film. We can further explore the film formation evolution from gel to final film by fitting the through-plane ionomer peak via the Teubner-Strey model to understand how the bicontinuous structure changes.[36-37] The ionomer peak is anisotropic; in-plane the intensity is very weak and does not exhibit the same dynamics observed through-plane (to see full GISAXS patterns please refer to Figure S6 in the SI). Thus, only the through-plane data is analyzed. Figure S8 plots extracted parameters for the Teubner-Strey model as a function of time for a water:nPA ratio dispersions, which are related to the hydrophilic domain spacing, correlation length of the domains, volume fractions, and scattering length contrast. Similar as to in the solution state, kinetics in the gel state proceed on a timescale proportional to the ratio of water to nPA. The LWD quickly approach their final domain spacing, and dry to the point at which no ionomer peak is visible (as evidenced by the large error bars). For HWD samples, the drying kinetics are slower, and the ionomer peak more slowly approaches its final values. Equilibration times for the Teubner-Strey fitting parameters are plotted in Figure S9 and show an increase in equilibration time with increasing water concentration.

At t = 200 s, the LWD were completely formed into a thin film, as demonstrated by the complete collapse of the ionomer peak (expected at~0.2 nm$^{-1}$) due to lack of contrast (see Figure 4). The films made from HWD, meanwhile, still exhibit a weak ionomer peak, indicating that some residual solvent remains. The 90% sample was measured out to 300 s with slight change in the ionomer peak. While the values have reached equilibrium values, residual solvent persists beyond the timescale of the experiment (see Figures S8 and S9 in the SI). Further drying beyond this is expected to cause a similar complete ionomer peak collapse. Final film thicknesses are shown in Table S2 in the SI.

At the above x-ray energy, absorbed water is needed to provide a contrast mechanism, and so differences in the final unhydrated structure cannot be probed. For this reason, the membrane structure experiments were performed at an energy near the sulfur K-edge to increase the electronic density contrast.

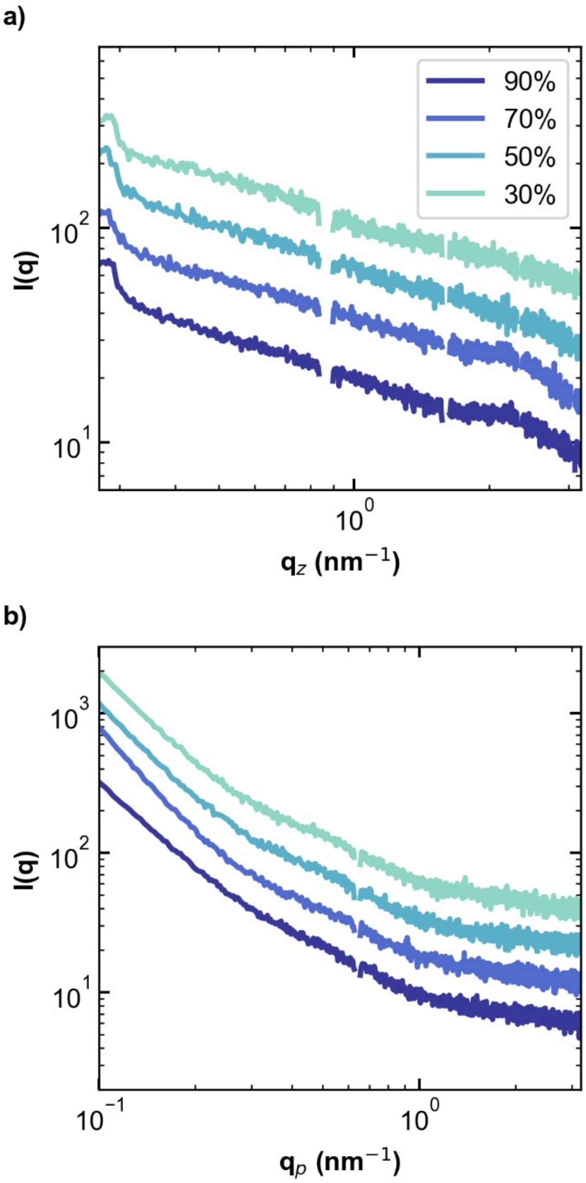

**Figure 4**. (a) Through-plane and (b) in-plane linecuts (offset for visual clarity) taken at the conclusion of film formation showing intensity (I) as a function of the scattering vector (q). Labels describe the weight percentage of water that makes up the dispersion solvent composition (the balance is n-propanol) from which these films were cast.

*Annealed Membranes.* To explore the effect of water:nPA ratio on membrane structure, membranes were prepared via solution-casting of dispersions containing the same solvent ratios as above. Because unannealed solution-cast membranes are extremely brittle[30, 32, 51] (free-standing films are very difficult to isolate), and may not be fully formed, they lack application relevance. Therefore, these membranes were annealed at 150°C for one hour following drying as the thermal annealing process is known to improve the membranes' mechanical properties. This improvement is hypothesized to be because of an increase in chain entanglements when Nafion is raised above its α-transition temperature.[32]

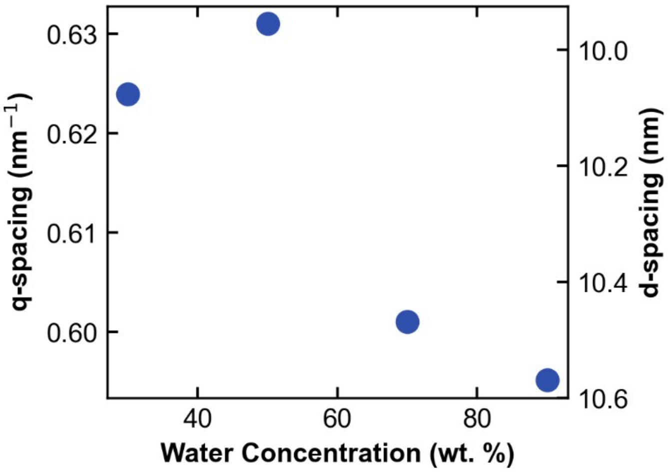

**Figure 5.** Inter-crystalline peak position (in reciprocal and real space) of the membranes as a function of the dispersion water concentration (balance n-propanol) at 2452 eV. Error bars are smaller than data points.

Annealed membranes were characterized using tender Wide-Angle X-ray Scattering (WAXS) at 2542 eV, to enhance scattering contrast in the film. These membranes were shot in vacuum, and while visible, the ionomer peak is very weak and does not display significant differences between samples. Interestingly, the inter-crystalline peak is quite strong at these energies. The inter-crystalline peak is indicative of how primary and secondary aggregates from solution have collapsed and arranged in the annealed film; the primary structure factor peak collapses into the inter-crystalline peak. Thus, it is representative of the network-like structure of the film. Figure 5 shows both the domain spacing (d-spacing, real space) and q-spacing (reciprocal space) as a function of dispersion water concentration from which the membranes were cast. The radially integrated scattering showing the inter-crystalline peak are shown in Figure S10 in the SI. There are clear differences between the water concentrations: membranes made from HWD exhibit a larger characteristic network size than those made from LWD. This suggests that the mesh size of the backbone network (and correspondingly the hydrophilic domain network) is larger for membranes made from HWD. While these differences are small, these domain spacing changes will likely be magnified upon hydration and will impact the transport properties of the membrane. Importantly, this difference due to dispersion provenance is present post-annealing in vacuum, when there is no residual solvent left. Thus, the changes in dispersion aggregation and film formation persist with thermal annealing and impact membrane and thin-film morphology at all length scales (see Figure 6).

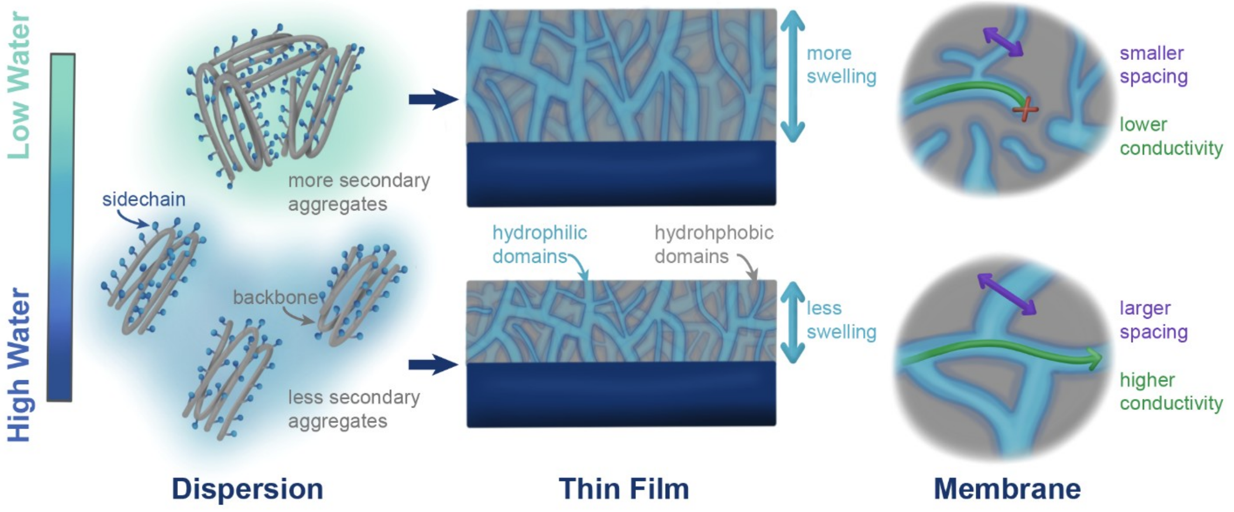

**Figure 6.** Proposed schematic depicting conclusions of data for dispersion aggregation, thin films, and membranes for high- and low-water concentrations. Features are not drawn to scale. Membrane diagram zooms into possible nanoscale/mesoscale structure (not meant to depict the entire membrane).

## Properties

It is important to understand how these different thin-film and membrane structures affect application-relevant properties: the transport and mechanical properties in PFSAs are a function of their hydration, making water content the most critical parameter to determine.[2]

*Thin Film.* For thin films, water uptake (or swelling) is measured using spectroscopic ellipsometry as a function of RH as shown in Figure 7. We investigate the impact of dispersion water:nPA ratio on both unannealed films (like those that were explored in the casting experiments above) as well as thin films of the same thickness that have been annealed at 150°C for one hour (the same annealing procedure used throughout this study for membranes).

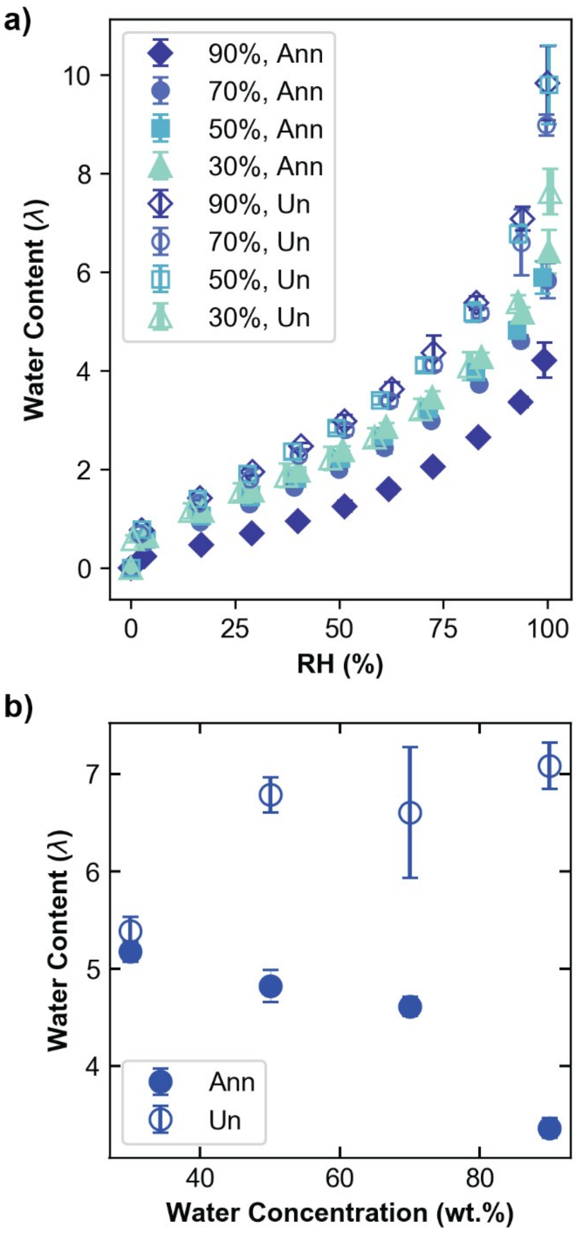

**Figure 7**. Thin-film (~145 nm thick on silicon) swelling measurements displaying water content ($\lambda$, mol water/mol $SO_3^-$) (a) as a function of relative humidity (RH). Labels describe the weight percentage of water that makes up the dispersion solvent composition (the balance is n-propanol) from which these films were cast. (b) Shows the swelling at 90% RH as a function of the

dispersion solvent. Closed symbols (●) denote annealed (Ann) films, and open symbols (○) denote unannealed (Un) films.

As Figure 7 displays, more water is absorbed by unannealed samples than annealed samples. This observation is supported by previous studies comparing unannealed and annealed Nafion thin films.[38] However, for unannealed films, the differences among the films made from HWD is almost nonexistent; only the film made from the 30% dispersion has a noticeable difference in swelling. It is possible that because these films are unannealed they revert to a pseudo-gel state at high hydration that is similar for all of them. These films are first exposed to 100% RH as a conditioning step and it is possible that this conditioning step wipes out differences in the original structure as they all swell with pure water, thus explaining why all but the 30% film (which would have the most different initial structure from a film cast from pure water) possess similar swelling behavior upon RH cycling. Previous work has shown that unannealed membranes dissolve in the presence of polar solvents,[30] thus supporting the idea that unannealed thin films may experience considerable swelling and reorganization upon exposure to 100% RH.

As opposed to the unannealed films, the annealed films do exhibit a trend with swelling as a function of the dispersion water concentration: swelling decreases as the water concentration in the dispersion the films were cast from increases. This trend suggests perhaps that the films have better chain entanglement, possibly due to the smaller secondary aggregates and a more regular arrangement of aggregates (as indicated by the stronger primary structure-factor peak) in the dispersion as the film forms. This morphology may lead to a more cohesive network, restricting swelling.[52]

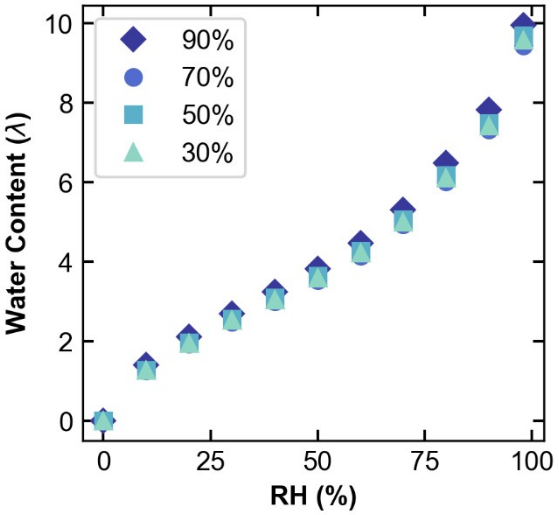

**Figure 8.** Membrane swelling measurements displaying water content ($\lambda$, mol water/mol $SO_3^-$) as a function of relative humidity (RH). Labels describe the weight percentage of water that makes up the dispersion solvent composition (the balance is n-propanol) from which these films were cast. Error bars are smaller than data points.

*Membrane.* As with the thin films, membrane water uptake was measured as shown in Figure 8. Unlike for the annealed thin films, the annealed membranes do not show a strong trend as a function of dispersion water concentration; perhaps the 90% film absorbs more water, but not significantly. Additional confinement effects experienced by the thin films may explain the difference in trend exhibited by the thin films versus the membranes. Confinement suppresses the water uptake in thin films to a regime that is comparable to the primary hydration of a membrane.[2, 38] For a fair comparison with thin-film hydration, the membrane residual water content is measured at 0% RH to determine the amount of water molecules strongly bound to the ionic groups in the solvation regime. Interestingly, the residual water in these membranes exhibits the same trend as the thin-film swelling: decreasing with increasing dispersion water concentration (see Figure S11 in SI). This suggests nanoscale changes in sidechain solvation and local water environment as dispersion water concentration varies. Thus, while dispersion effects are dominant in the entire hydration range for thin films, they are present mostly in the primary hydration environment for membranes.

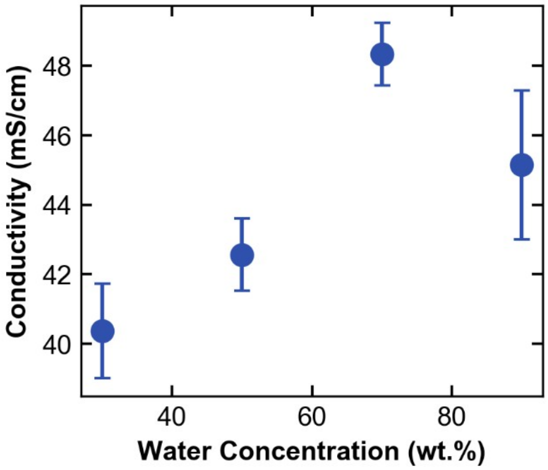

**Figure 9**. In-plane conductivity of membranes prepared from dispersions of varying water concentration (balance n-propanol).

While we do know that the mesh size of the network is different among these membranes as evidenced in Figure 5, we cannot probe the network connectivity/tortuosity in scattering experiments. One way we can probe connectivity, however, is by measuring membrane conductivity; previous work has shown directly that conductivity (a macroscale property) is controlled by nano- and mesoscale properties like solvation and network connectivity.[53] The results of in-plane membrane conductivity in DI water are given in Figure 9. The measured conductivities fall in the expected range considering values exhibited by commercial Nafion and other solvent-cast Nafion systems.[2, 29, 31] Membrane conductivity increases with increasing dispersion water concentration, with a peak conductivity in the 70% sample. Why the 70% membrane possesses the highest conductivity is not immediately obvious. However, it likely is a result of a balance between the more swollen dispersion conformations produced by mixed water/propanol solvents[21], and the enhanced ordering exhibited by the HWD. Additional work to determine this is required. Regardless, the membranes produced from the HWD clearly show enhanced conductivities over those prepared from the LWD, despite possessing similar water contents (see Figure 8). The conductivity data therefore suggests that the network organization is different (and better) in the membranes made from the HWD, particularly because water volume fraction is the same with changing conductivity. This demonstrates that the connectivity effects seen in the annealed thin films are also present the in membranes.

## Structure-Property Implications

Figure 6 schematically interprets the above data. The dispersion aggregation behavior changes as a function of water concentration, which affects how the films coalesce and the resultant nanoscale structure that in turn impacts macroscopic, observable properties.

The interactions between Nafion aggregates and the regularity of their ordering increases as water concentration in the dispersion increases. Furthermore, the equilibrium time to gelation and final formed film increases with increasing water concentration. However, it should be noted that there will be preferential nPA evaporation, and that the water:nPA ratio changes during the drying process.[32] Despite this, it is clear that the initial dispersion concentrations are deterministic of film formation process: timescales do not scale linearly with water concentration, and the intensities of the structure factor peaks are different across the four solvent ratios. Data cannot simply be normalized to water concentration and correlated with evaporation rate. These dispersion aggregation ordering differences are clearly translated to the membrane: changes in inter-crystalline peak position reflect the primary structure factor peak in solution.

Upon annealing, thin films cast from the HWD exhibit less swelling, and membranes show a larger spacing between backbone regions. Despite this larger spacing, membranes show the same water content, suggesting better network connectivity/aggregate packing, perhaps due to the greater regularity of aggregates as the film forms. It is unclear how the varying water:nPA ratio affects the durability and mechanical properties of the ionomer, but from a transport-property perspective, the HWD films are preferable (although the longer equilibration time required for film formation may not be desirable at manufacturing scales).

Understanding specifically what is happening during the annealing process requires further investigation. It is believed that raising the membranes above their α-transition temperature disentangles the ionic domains and allows for rearrangement of the ionic network.[2] However, the backbone crystallite regions should remain relatively unaffected; it has been demonstrated there is little change with crystallinity at these temperatures (although there can be significant change at much higher temperatures).[54] Given this and the above data, it seems that the thermal annealing process here preserves the backbone domains and aggregate structures that coalesce during film formation. While the ionic domains can reorient and increase chain entanglement, meso- and macroscale changes to the network structure seem unlikely.

Therefore, annealing locks in the differences in film formation caused by the varying solvent composition in the dispersion, while the unannealed films can possibly eliminate their solvent history upon sufficient cycling in pure solvents (based on the swelling data from the unannealed films). Both findings have interesting implications for CLs in PEM fuel cells, electrolyzers, and similar devices. These CLs are created through different fabrication processes. Gas-diffusion electrodes (where the CL is deposited onto the diffusion media) are often hot pressed to the membrane at elevated temperatures to form a membrane-electrode assembly with minimized ohmic losses. Catalyst-coated membranes (in which the CL is deposited directly onto the membrane) on the other hand are often not hot pressed. Based on these findings, the differences between these two processes may further be compounded by the high-temperature treatment step: hot-pressed samples may retain dispersion solvent differences, while samples that were not hot pressed may not. Furthermore, these devices often go through a temperature/RH/voltage break-in protocol before initial operation to condition the electrodes. Particularly for electrodes that have not been subjected to elevated temperatures, the ionomer swelling/reorganization during this break-in cycle is critical and may help explain some of the changes observed during break-in.

However, even post-break in, the effects of dispersion solvent are likely to remain whether the CL was hot-pressed or not. These films form quite differently, and likely will impact (and be impacted by) how the catalyst particles agglomerate. One could imagine the greater density of secondary aggregates in low-water-concentration inks affects how agglomerates of particles forms as compared to the lower density of aggregates in high-water-concentration inks. Indeed, ink-level studies have shown that water concentration changes catalyst/ionomer aggregation behavior,[4] and that low-water-concentration inks are less sensitive to ionomer content than high-water-concentration inks are,[18] thereby suggesting that the changing ionomer/solvent interaction drives differing aggregation modes. Therefore, even though after RH cycling the unannealed thin films may behave similarly, large-scale catalyst particle reorganization is unlikely: the impact of solvent during CL formation will still be critical in controlling device performance.

## CONCLUSIONS

In this study, the effects of solvent composition on PFSA states (dispersion, thin film, membrane) were examined. It was shown how dispersion solvent effects persist across the various states, length scales, and even annealing conditions. Specifically, we investigated the impact of water:nPA ratio on how thin films form from dispersions using time-resolved GISAXS, extended this understanding to probe structure in membranes with WAXS at tender X-ray energies, and then investigated the impact of these structures on thin-film swelling (of both annealed and unannealed films) and membrane swelling and conductivity. Notably, the dispersion water:nPA ratio altered how the films form by changing the timescale for the formation process, the strength of interactions of the dispersion aggregates, and how these aggregates come together within the film network. Membranes also demonstrated evidence of the impact of solvent: changing network spacing as a function of the solvent from which the membranes were cast. Furthermore, thin films prepared from high-water-concentration dispersions (HWD) exhibited less swelling than those prepared from low-water-concentration dispersions (LWD). Similarly, membranes cast from HWD had greater conductivities than LWD membranes. This structural data, coupled with the property data, suggest that HWD exhibit stronger aggregate interactions upon film formation for both membranes and thin films, and that these stronger interactions likely yield better network connectivity, thus explaining the trends for conductivity and water uptake. However, to probe network connectivity/tortuosity definitively, additional energy-resolved scattering work or cryo-electron microscopy is necessary to map sulfur/water channel distributions. As noted, thermal annealing seemed to preserve solvent-ratio effects rather than erase them. Unannealed thin films exhibited much weaker variation in properties between different water concentrations. Additionally, swelling-trend discrepancies between thin films and membranes were likely due to confinement effects. These confinement effects are expected to be further impacted by substrate identity; additional research into how these solvent/ionomer interactions manifest on different substrates is required. Furthermore, the degree to which dispersion solvent impacts thin films and membranes post annealing is expected to change as a function of annealing temperature. This work presents an important step in understanding solvent/ionomer interactions. Dispersion-level interactions persist across all length scales, affect film formation and properties, and are maintained upon thermal annealing. With this knowledge, one can begin to understand how solvent choice nuances catalyst layer inks, CL microstructure, membrane properties, and other device-level metrics. More importantly, one can contemplate engineering dispersions and inks for specific PFSA properties, thus enabling higher-performing devices.

ASSOCIATED CONTENT

**Supporting Information**. Nafion structure, form factor fits, 2D GISAXS patterns, full viscosity profiles, Teubner-Strey fitting, WAXS data, membrane swelling residual water

AUTHOR INFORMATION

**Corresponding Author**

*Sarah A. Berlinger: sarah_berlinger@berkeley.edu

**Present Addresses**

†Polymer Processing Group, National Institute of Standards and Technology, Gaithersburg, MD, 20899

ACKNOWLEDGMENT

The authors would like to thank Dr. Gregory Su and Dr. Andrew Crothers for helpful discussions. This work was mainly funded under the Fuel Cell Performance and Durability Consortium (FC-PAD), by the Fuel Cell Technologies Office (FCTO), of the office of the Energy Efficiency and Renewable Energy (EERE), of the U. S. Department of Energy under contract number DE-AC02-05CH1123. *In situ* GISAXS work was conducted at beamline 7.3.3 at the Advanced Light Source (ALS), supported by the Office of Science, Office of Basic Energy Sciences, of the U.S. Department of Energy (Contract No. DE-AC02-05CH11231). WAXS data was collected at the Soft Matter Interfaces (SMI) Beamline 12-ID of the National Synchrotron Light Source II, a U.S. Department of Energy (DOE) Office of Science User Facility operated for the DOE Office of Science by Brookhaven National Laboratory under Contract No. DE-SC0012704. S.A.B acknowledges support from the Graduate Research Fellowship Program by the National Science Foundation under Grant No. DGE 1752814.

**REFERENCES**

1. Holdcroft, S., Fuel Cell Catalyst Layers: A Polymer Science Perspective. *Chem. Mater.* **2014,** *26* (1), 381-393.
2. Kusoglu, A.; Weber, A. Z., New Insights into Perfluorinated Sulfonic-Acid Ionomers. *Chem. Rev.* **2017,** *117* (3), 987-1104.
3. Hatzell, K. B.; Dixit, M. B.; Berlinger, S. A.; Weber, A. Z., Understanding inks for porous-electrode formation. *J. Mater. Chem. A* **2017,** *5* (39), 20527-20533.
4. Van Cleve, T.; Khandavalli, S.; Chowdhury, A.; Medina, S.; Pylypenko, S.; Wang, M.; More, K. L.; Kariuki, N.; Myers, D. J.; Weber, A. Z.; Mauger, S. A.; Ulsh, M.; Neyerlin, K. C., Dictating Pt-Based Electrocatalyst Performance in Polymer Electrolyte Fuel Cells, from Formulation to Application. *ACS Appl. Mater. Interfaces* **2019,** *11* (50), 46953-46964.
5. Osmieri, L.; Wang, G.; Cetinbas, F. C.; Khandavalli, S.; Park, J.; Medina, S.; Mauger, S. A.; Ulsh, M.; Pylypenko, S.; Myers, D. J.; Neyerlin, K. C., Utilizing ink composition to tune bulk-electrode gas transport, performance, and operational robustness for a Fe–N–C catalyst in polymer electrolyte fuel cell. *Nano Energy* **2020,** *75*, 104943.
6. Shin, S. J.; Lee, J. K.; Ha, H. Y.; Hong, S. A.; Chun, H. S.; Oh, I. H., Effect of the catalytic ink preparation method on the performance of polymer electrolyte membrane fuel cells. *J. Power Sources* **2002,** *106* (1–2), 146-152.
7. Xie, Z.; Navessin, T.; Zhao, X.; Adachi, M.; Holdcroft, S.; Mashio, T.; Ohma, A.; Shinohara, K., Nafion Ionomer Aggregation and its Influence on Proton Conduction and Mass Transport in Fuel Cell Catalyst Layers. *ECS Trans.* **2008,** *16* (2), 1811-1816.
8. Doo, G.; Lee, J. H.; Yuk, S.; Choi, S.; Lee, D.-H.; Lee, D. W.; Kim, H. G.; Kwon, S. H.; Lee, S. G.; Kim, H.-T., Tuning the Ionomer Distribution in the Fuel Cell Catalyst Layer with Scaling the Ionomer Aggregate Size in Dispersion. *ACS Appl. Mater. Interfaces* **2018,** *10* (21), 17835-17841.
9. Ngo, T. T.; Yu, T. L.; Lin, H.-L., Influence of the composition of isopropyl alcohol/water mixture solvents in catalyst ink solutions on proton exchange membrane fuel cell performance. *J. Power Sources* **2013,** *225*, 293-303.
10. Uchida, M.; Aoyama, Y.; Eda, N.; Ohta, A., New Preparation Method for Polymer-Electrolyte Fuel Cells. *J. Electrochem. Soc.* **1995,** *142* (2), 463-468.
11. Huang, D. C.; Yu, P. J.; Liu, F. J.; Huang, S. L.; Hsueh, K. L.; Chen, Y. C.; Wu, C. H.; Chang, W. C.; Tsau, F. H., Effect of Dispersion Solvent in Catalyst Ink on Proton Exchange Membrane Fuel Cell Performance. *Int. J. Electrochem. Sci.* **2011,** *6* (7), 2551-2565.
12. Sharma, R.; Grahl-Madsen, L.; Andersen, S. M., Influence of dispersion media on Nafion® ionomer distribution in proton exchange membrane fuel cell catalyst carbon support. *Materials Chemistry and Physics* **2019,** *226*, 66-72.
13. Kim, T.-H.; Yi, J.-Y.; Jung, C.-Y.; Jeong, E.; Yi, S.-C., Solvent effect on the Nafion agglomerate morphology in the catalyst layer of the proton exchange membrane fuel cells. *Int. J. Hydrogen Energy* **2017,** *42* (1), 478-485.
14. Orfanidi, A.; Rheinländer, P. J.; Schulte, N.; Gasteiger, H. A., Ink Solvent Dependence of the Ionomer Distribution in the Catalyst Layer of a PEMFC. *J. Electrochem. Soc.* **2018,** *165* (14), F1254-F1263.
15. Lee, J. H.; Doo, G.; Kwon, S. H.; Choi, S.; Kim, H.-T.; Lee, S. G., Dispersion-Solvent Control of Ionomer Aggregation in a Polymer Electrolyte Membrane Fuel Cell. *Scientific Reports* **2018,** *8* (1), 10739.

16. Ngo, T. T.; Yu, T. L.; Lin, H.-L., Nafion-based membrane electrode assemblies prepared from catalyst inks containing alcohol/water solvent mixtures. *J. Power Sources* **2013,** *238*, 1-10.
17. Yang, F.; Xin, L.; Uzunoglu, A.; Stanciu, L.; Ilavsky, J.; Son, S.; Xie, J., Investigation of Solvent Effects on the Dispersion of Carbon Agglomerates and Nafion Ionomer Particles in Catalyst Inks Using Ultra Small Angle X-Ray Scattering Method. *ECS Trans.* **2016,** *75* (14), 361-371.
18. Berlinger, S. A.; McCloskey, B. D.; Weber, A. Z., Inherent Acidity of Perfluorosulfonic Acid Ionomer Dispersions and Implications for Ink Aggregation. *J. Phys. Chem. B.* **2018,** *122* (31), 7790-7796.
19. Dixit, M. B.; Harkey, B. A.; Shen, F.; Hatzell, K. B., Catalyst Layer Ink Interactions That Affect Coatability. *J. Electrochem. Soc.* **2018,** *165* (5), F264-F271.
20. Shukla, S.; Bhattacharjee, S.; Weber, A. Z.; Secanell, M., Experimental and Theoretical Analysis of Ink Dispersion Stability for Polymer Electrolyte Fuel Cell Applications. *J. Electrochem. Soc.* **2017,** *164* (6), F600-F609.
21. Welch, C.; Labouriau, A.; Hjelm, R.; Orler, B.; Johnston, C.; Kim, Y. S., Nafion in Dilute Solvent Systems: Dispersion or Solution? *ACS Macro. Lett.* **2012,** *1* (12), 1403-1407.
22. Gebel, G.; Loppinet, B., Colloidal structure of ionomer solutions in polar solvents. *J. Mol. Struct.* **1996,** *383* (1), 43-49.
23. Loppinet, B.; Gebel, G., Rodlike Colloidal Structure of Short Pendant Chain Perfluorinated Ionomer Solutions. *Langmuir* **1998,** *14* (8), 1977-1983.
24. Loppinet, B.; Gebel, G.; Williams, C. E., Small-Angle Scattering Study of Perfluorosulfonated Ionomer Solutions. *J. Phys. Chem. B.* **1997,** *101* (10), 1884-1892.
25. Aldebert, P.; Gebel, G.; Loppinet, B.; Nakamura, N., Polyelectrolyte effect in perfluorosulfonated ionomer solutions. *Polymer* **1995,** *36* (2), 431-434.
26. Lee, S.-J.; Yu, T. L.; Lin, H.-L.; Liu, W.-H.; Lai, C.-L., Solution properties of nafion in methanol/water mixture solvent. *Polymer* **2004,** *45* (8), 2853-2862.
27. Tarokh, A.; Karan, K.; Ponnurangam, S., Atomistic MD Study of Nafion Dispersions: Role of Solvent and Counterion in the Aggregate Structure, Ionic Clustering, and Acid Dissociation. *Macromolecules* **2020,** *53* (1), 288-301.
28. Lin, H.-L.; Yu, T. L.; Huang, C.-H.; Lin, T.-L., Morphology study of Nafion membranes prepared by solutions casting. *J. Polym. Sci., Part B: Polym. Phys.* **2005,** *43* (21), 3044-3057.
29. Ma, C.-H.; Yu, T. L.; Lin, H.-L.; Huang, Y.-T.; Chen, Y.-L.; Jeng, U. S.; Lai, Y.-H.; Sun, Y.-S., Morphology and properties of Nafion membranes prepared by solution casting. *Polymer* **2009,** *50* (7), 1764-1777.
30. Moore, R. B.; Martin, C. R., Chemical and Morphological Properties of Solution-Cast Perfluorosulfonate Ionomers. *Macromolecules* **1988,** *21* (5), 1334-1339.
31. Silva, R. F.; De Francesco, M.; Pozio, A., Solution-cast Nafion® ionomer membranes: preparation and characterization. *Electrochim. Acta* **2004,** *49* (19), 3211-3219.
32. Kim, Y. S.; Welch, C. F.; Hjelm, R. P.; Mack, N. H.; Labouriau, A.; Orler, E. B., Origin of Toughness in Dispersion-Cast Nafion Membranes. *Macromolecules* **2015,** *48* (7), 2161-2172.
33. Dudenas, P. J.; Kusoglu, A., Evolution of Ionomer Morphology from Dispersion to Film: An in Situ X-ray Study. *Macromolecules* **2019,** *52* (20), 7779-7785.

34. Liu, F.; Ferdous, S.; Schaible, E.; Hexemer, A.; Church, M.; Ding, X.; Wang, C.; Russell, T. P., Fast printing and in situ morphology observation of organic photovoltaics using slot-die coating. *Advanced materials (Deerfield Beach, Fla.)* **2015,** *27* (5), 886-91.

35. Kline, S., Reduction and analysis of SANS and USANS data using IGOR Pro. *Journal of Applied Crystallography* **2006,** *6* (39), 895-900.

36. Teubner, M.; Strey, R., Origin of the scattering peak in microemulsions. *The Journal of Chemical Physics* **1987,** *87* (5), 3195-3200.

37. Chen, S. H.; Chang, S. L.; Strey, R. In *On the interpretation of scattering peaks from bicontinuous microemulsions*, Darmstadt, Steinkopff: Darmstadt, 1990; pp 30-35.

38. Kusoglu, A.; Kushner, D.; Paul, D. K.; Karan, K.; Hickner, M. A.; Weber, A. Z., Impact of Substrate and Processing on Confinement of Nafion Thin Films. *Advanced Functional Materials* **2014,** *24* (30), 4763-4774.

39. Dishari, S. K.; Hickner, M. A., Antiplasticization and Water Uptake of Nafion Thin Films. *ACS Macro Lett.* **2012,** *1* (2), 291-295.

40. Kongkanand, A., Interfacial Water Transport Measurements in Nafion Thin Films Using a Quartz-Crystal Microbalance. *J Phys Chem C* **2011,** *115* (22), 11318-11325.

41. Paul, D. K.; Fraser, A.; Karan, K., Towards the understanding of proton conduction mechanism in PEMFC catalyst layer: Conductivity of adsorbed Nafion films. *Electrochemistry Communications* **2011,** *13* (8), 774-777.

42. Eastman, S. A.; Kim, S.; Page, K. A.; Rowe, B. W.; Kang, S.; Soles, C. L.; Yager, K. G., Effect of Confinement on Structure, Water Solubility, and Water Transport in Nafion Thin Films. *Macromolecules* **2012,** *45* (19), 7920-7930.

43. Gebel, G.; Lambard, J., Small-Angle Scattering Study of Water-Swollen Perfluorinated Ionomer Membranes. *Macromolecules* **1997,** *30* (25), 7914-7920.

44. Takamatsu, T.; Eisenberg, A., Densities and expansion coefficients of nafion polymers. *J. Appl. Polym. Sci.* **1979,** *24* (11), 2221-2235.

45. Zhernenkov, M.; Canestrari, N.; Chubar, O.; DiMasi, E. In *Soft matter interfaces beamline at NSLS-II: geometrical ray-tracing vs. wavefront propagation simulations*, September 01, 2014; 2014; p 92090G.

46. Pandolfi, R. J.; Allan, D. B.; Arenholz, E.; Barroso-Luque, L.; Campbell, S. I.; Caswell, T. A.; Blair, A.; Carlo, F. D.; Fackler, S.; Fournier, A. P.; Freychet, G.; Fukuto, M.; Gürsoy, D.; Jiang, Z.; Krishnan, H.; Kumar, D.; Kline, R. J.; Li, R.; Liman, C.; Marchesini, S.; Mehta, A.; N'Diaye, A. T.; Parkinson, D. Y.; Parks, H.; Pellouchoud, L. A.; Perciano, T.; Ren, F.; Sahoo, S.; Strzalka, J.; Sunday, D.; Tassone, C. J.; Ushizima, D.; Venkatakrishnan, S.; Yager, K. G.; Zwart, P.; Sethian, J. A.; Hexemer, A., *Xi-cam:* a versatile interface for data visualization and analysis. *Journal of Synchrotron Radiation* **2018,** *25*, 1261-1270.

47. Kusoglu, A.; Savagatrup, S.; Clark, K. T.; Weber, A. Z., Role of Mechanical Factors in Controlling the Structure-Function Relationship of PFSA Ionomers. *Macromolecules* **2012,** *45* (18), 7467-7476.

48. Kusoglu, A.; Weber, A. Z., Water Transport and Sorption in Nafion Membrane. In *Polymers for Energy Storage and Delivery: Polyelectrolytes for Batteries and Fuel Cells*, American Chemical Society: 2012; Vol. 1096, pp 175-199.

49. Scribner *BekkTech's Procedures For Performing In-Plane Membrane Conductivity Testing*

50. Dealy, J. M.; Wissbrun, K. F., *Melt Rheology and Its Role in Plastics Processing*. Springer: 1990.

51. Gebel, G.; Aldebert, P.; Pineri, M., Structure and related properties of solution-cast perfluorosulfonated ionomer films. *Macromolecules* **1987,** *20* (6), 1425-1428.

52. Kusoglu, A.; Savagatrup, S.; Clark, K. T.; Weber, A. Z., Role of Mechanical Factors in Controlling the Structure–Function Relationship of PFSA Ionomers. *Macromolecules* **2012,** *45* (18), 7467-7476.

53. Crothers, A. R.; Radke, C. J.; Weber, A. Z., Impact of Nano- and Mesoscales on Macroscopic Cation Conductivity in Perfluorinated-Sulfonic-Acid Membranes. *J. Phys. Chem. C.* **2017,** *121* (51), 28262-28274.

54. Gao, X.; Yamamoto, K.; Hirai, T.; Uchiyama, T.; Ohta, N.; Takao, N.; Matsumoto, M.; Imai, H.; Sugawara, S.; Shinohara, K.; Uchimoto, Y., Morphology Changes in Perfluorosulfonated Ionomer from Thickness and Thermal Treatment Conditions. *Langmuir* **2020,** *36* (14), 3871-3878.

**TOC Graphic:**

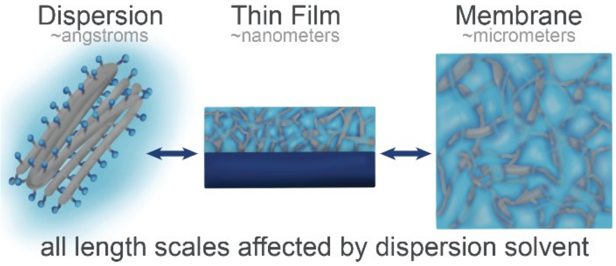

For Table of Contents Only